Growth of mica porphyroblasts under low-grade metamorphism – A Taiwanese case using *in-situ* ^{40}Ar/^{39}Ar laser microprobe dating

CrossMark

Chih-Tung Chen [a, *], Yu-Chang Chan [b], Ching-Hua Lo [a], Chia-Yu Lu [a]

[a] *Department of Geosciences, National Taiwan University, No. 1, Sec. 4, Roosevelt Road, Taipei, Taiwan, ROC*
[b] *Institute of Earth Sciences, Academia Sinica, No. 128, Sec. 2, Academia Road, Nangang, Taipei, Taiwan, ROC*

ARTICLE INFO

ABSTRACT

Mica porphyroblasts, a common metamorphic microstructure, are analyzed in the slate belt of northern Taiwan where large fish-like growths are found within a meta-pyroclastics. With constraints on the time-temperature history from deposition through peak metamorphic state to exhumation, *in-situ* ^{40}Ar/^{39}Ar laser microprobe dating was carried out on muscovite and corrensite fibers of mm-scale mica porphyroblasts grown on a pressure-solution seam. Because the peak metamorphic temperature and the porphyroblast formation condition (~250 °C) remained far below the closure temperature of the K-Ar radioisotope system in muscovite, and the absence of muscovite in the mafic protolith, the dating results likely document the growth of the mica porphyroblast fabrics. The syn-kinematic nature of the analyzed porphyroblasts is confirmed by the ~6 to ~2.5 Ma growth ages, suggesting that the host rock was continuously deformed during the earlier two-thirds of the Taiwan Orogeny. The pattern of fiber growth, in contrast to outward-decreasing ages normally observed in peripheral recrystallization, appears random and resembles void fills in boudin openings. We postulate that syntaxial crack-seal following tensile micro-boudinage, along with slips on sub-grain boundaries, as a viable mechanism for the development of mica porphyroblasts and fish especially in lower-grade metamorphic rocks.

© 2016 Elsevier Ltd. All rights reserved.

1. Introduction

Mica aggregates grown along foliation, including mica fish and porphyroblasts, are common microstructures in metamorphic rocks which possess important clues to the conditions of related deformation (Passchier and Trouw, 2005). They are postulated to develop through bending and internal deformation of existing porphyroclasts (ten Grotenhuis et al., 2003; Mukherjee, 2011), or strain fringe-like peripheral precipitation (Mulch et al., 2005) and even crack-seal processes (Clark and Fisher, 1995; Barker, 2002). The associated new growth allows direct documentation of the kinematic history of the mica aggregates, crucial in understanding the formation of the host shear zones or cleavage, by *in-situ* dating methods (e.g. Wells et al., 2008). However, this task is seldom achievable in high-grade mylonitic zones where mica fish are most abundant, as the relevant isotopic systems for dating muscovite fibers are usually breached due to the high temperature during mylonitization, thus yielding only cooling ages (Hodges, 2014). Better constraints may come from lower-grade terrains where the concerned radioisotope systems remain closed. In these terrains, unless unique correlations exist between mica grain size and syn-kinematic new growth (e.g. Fitz-Diaz and van der Pluijm, 2013), cleavage dating is particularly challenging in finding mica growth fibers large enough for structure-specific *in-situ* dating (Chan et al., 2000; Schneider et al., 2013). In this study an exceptional case of foliation mica porphyroblast growth in Taiwanese slate, resembling mica fish development under lower greenschist brittle-ductile transitional environment, is analyzed by *in-situ* ^{40}Ar/^{39}Ar laser microprobe dating. The results indicate that these microstructures may be active for long periods within an orogeny, and a crack-seal mechanism, combining brittle boudinage and void precipitation, may be central in the formation of mica porphyroblasts and fish under lower temperature conditions.

2. Geological background

The island of Taiwan is the result of mountain building by the ongoing convergence between the Eurasian Plate and the

* Corresponding author. Department of Geosciences, National Taiwan University, No. 1, Sec. 4, Roosevelt Road, Taipei 106, Taiwan, ROC.
E-mail address: kthomasch@gmail.com (C.-T. Chen).

Philippine Sea Plate (Suppe, 1981). The Chinese continental margin has been bulldozed by the Luzon Arc since latest Miocene time, and the obliquity between these colliding elements leads to the characteristic temporal-spatial relationship where moving northwards is equivalent to more advanced stages of orogen evolution (Suppe, 1984; Teng, 1990). The Taiwanese slate terrain, sandwiched between the foreland piedmont fold-thrust belt and the exhumed basement complex, constitutes the crest of the mountain belt and outcrops over half of the area of the Central Range (Fig. 1A). The western part of the slate terrain, the Hsuehshan Range, consists of metamorphosed rift sequence that underlies the platform sediment of the passive margin (Teng and Lin, 2004) and resembles a large-scale pop-up structure (Clark et al., 1993). The analyzed sample with extraordinary foliation mica growth, the NCIH-B2 sample of the mafic Sule Bridge Pyroclastics, is contained in the upper part of the margin succession in the northern Hsuehshan Range (Yang and Shau, 1988). In the following section, an introduction is given to the geology of the northern Hsuehshan Range and the geologic and structural context of the NCIH-B2 sample.

2.1. The northern Hsuehshan Range

The sediments of the northern Hsuehshan Range were accumulated in eastward-deepening half-graben formed in response to the opening of the South China Sea (Teng and Lin, 2004). From bottom to top, they are divided as follows (Fig. 1B): the Eocene Hsitsun Formation containing phyllitic slate and intercalated meta-sandstone layers, the Eocene-Oligocene Szeleng Formation with thick stratal intervals of quartzitic arenite to conglomerate, the Oligocene Kankou Formation, which consists of massive slate with rare sandstone, the Oligocene Tsuku Sandstone as a prominent arenite, the Oligocene Tatungshan Formation of argillite and sandstone interlayers, and the uppermost Miocene Sule Formation in which argillite alternates with calcareous sandstones. The Sule Formation correlates to the lower to upper Miocene sequences found in the un-metamorphosed Western Foothills, suggesting lateral continuation and consistency of deposition and facies associations at that time. In the eastern part of northern Hsuehshan Range, the Oligocene sediments, including the Kankou, Tsuku and Tatungshan formations become fine-grained and are collectively mapped as the Paling Formation. The Sule Bridge Pyroclastics exposure is conformable within the upper section of the Tatungshan Formation. The Miocene strata above were at most 2 km in total thickness, and the entire exposed section from Eocene was about 6 km thick in the northern Hsuehshan Range (Teng, 1992).

The rift graben on the external portions of the Chinese continental margin were inverted during the Neogene Taiwan Orogeny, and the sedimentary succession of the northern Hsuehshan Range was deformed into a series of NE-trending NW-vergent fault-fold structures and thrust over the Western Foothills along the Chuchih Fault (Chen et al., 2011). The NCIH-B2 sample is situated on the eastern limb of one of the major fold, the Chatienshan Anticline (Fig. 1B). The Hsuehshan Range is relatively uplifted against the Backbone Range to the east along the subvertical E-vergent Lishan Fault (Beyssac et al., 2007; Chen et al., 2011) which has a complex kinematic history (Clark et al., 1993; Lee et al., 1997). Slaty cleavage is developed in all rocks SE of the Junghua Dam on the outer limb of the Chatienshan Anticline (the 'onset of cleavage' in Fig. 2B) and generally strikes NE and dips steeply or is vertical, while the Oligo-Miocene indurate argillite in the western Hsuehshan Range possess
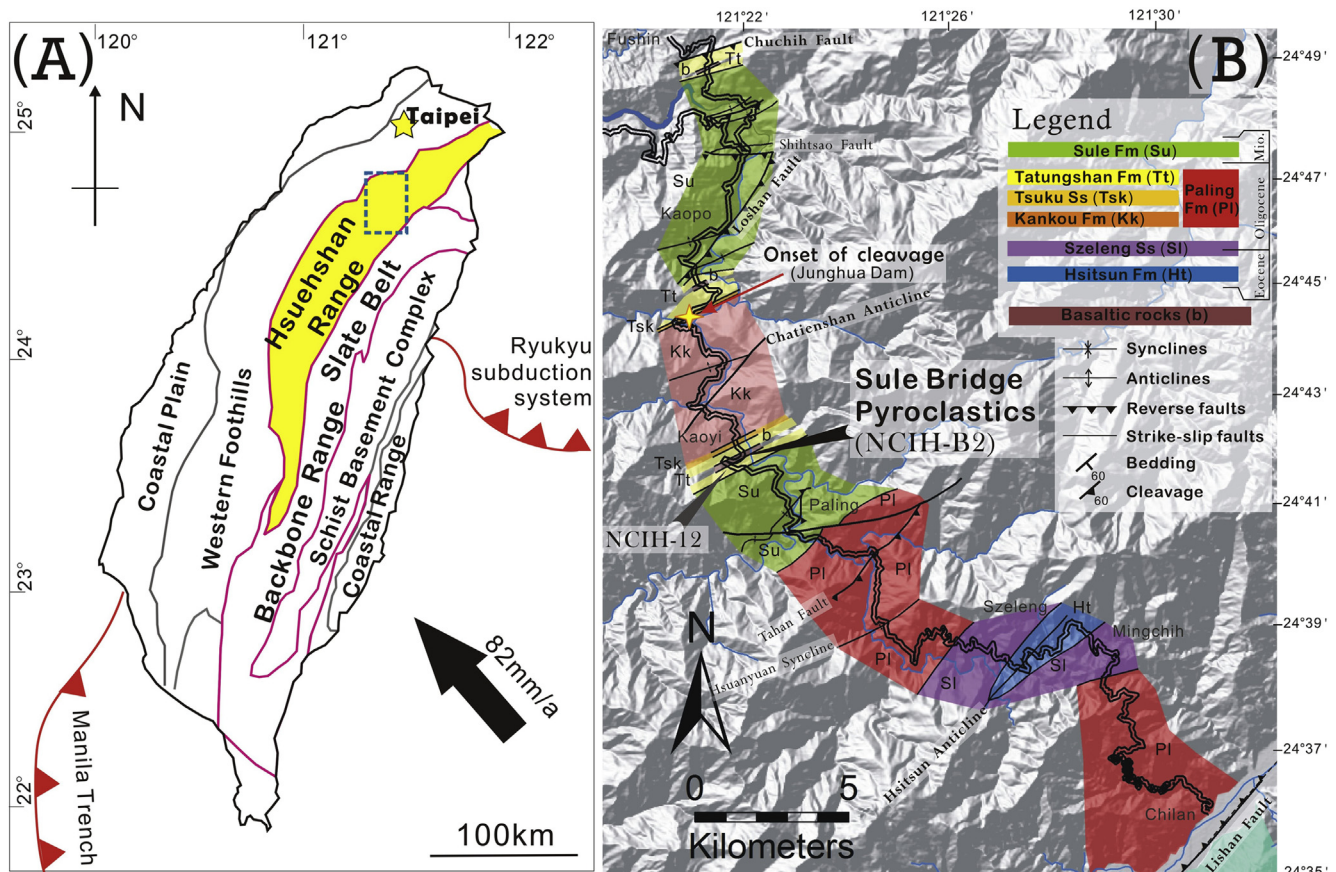

Fig. 1. A: Outline of major tectonic units in Taiwan. B: Geologic strip map along the North Cross Island Highway.
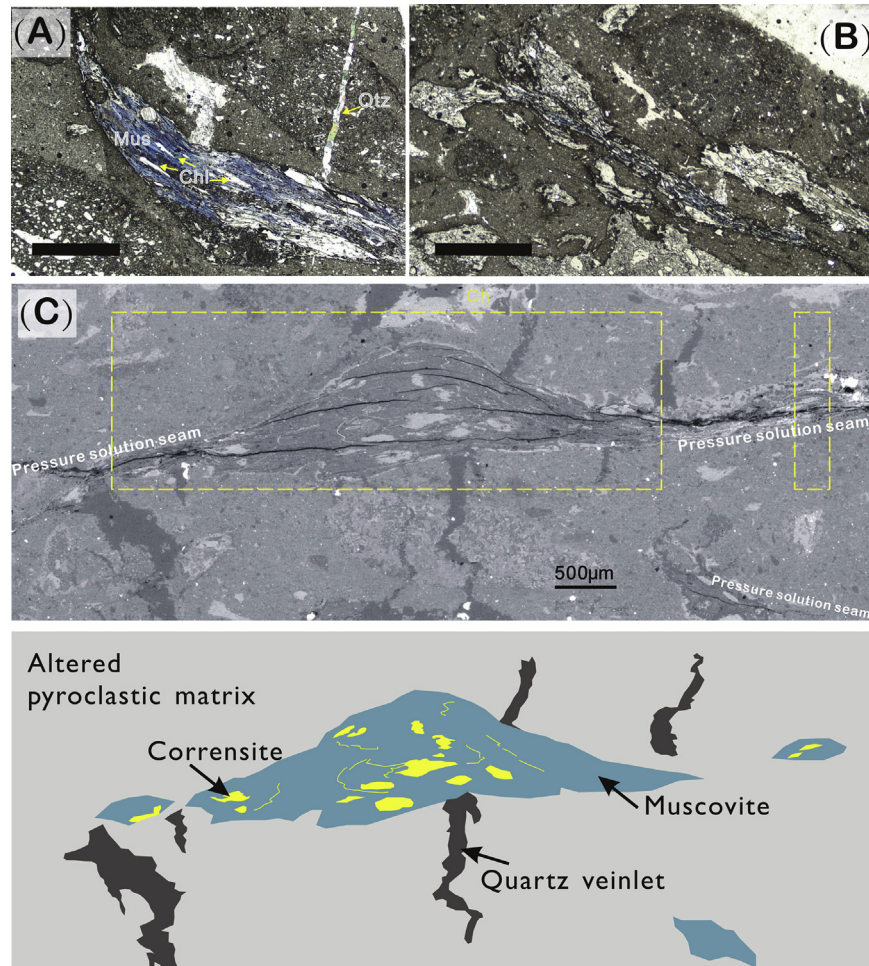
Fig. 2. A and B: Photomicrographs of the NCIH-B2 body showing large fish-like mica porphyroblasts grown along pressure solution seams. Cross-polarized light; scale bar = 1 mm. C: BSE image of the NCIH-B2 sample exhibiting mica porphyroblasts along a pressure solution seam, and simple sketch demonstrating the spatial distribution of muscovite, corrensite, quartz veinlet as well as altered pyroclastic matrix. Note the absence of simple shear deformation on porphyroblast shapes, neighboring grains and veinlets. Areas shown in Fig. 3 are marked.

only pencil cleavage. The rocks in the Hsuehshan Range are assigned to prehnite-pumpellyite grade with a greenschist facies core in the eastern part (Clark et al., 1993; Chen and Wang, 1995; Beyssac et al., 2007; Chen et al., 2011). Based on the thermokinematic history of the metasediments, the northern Hsuehshan Range possesses signs of synorogenic metamorphism overprinting basin burial diagenesis (Chen et al., 2011). As the special space-time association of the Taiwan Orogen implies, the northern Hsuehshan Range units were overridden by their central-southern counterparts during the foreland-ward advance and expansion of the orogenic wedge, and their exhumation to the land surface in the north was due to the longer history of tectonic evolution and denudation (Chen et al., 2011). At present, the northern Hsuehshan Range is experiencing waning collision to post-collisional processes (Shyu et al., 2005).

2.2. The NCIH-B2 sample

The NCIH-B2 sample is taken from an outcrop of the Sule Bridge Pyroclastics on the eastern limb of the Chatienshan Anticline, within the latest Oligocene Tatungshan Formation (Fig. 1B). The pyroclastics is mafic in composition with a prehnite-pumpellyite to greenschist facies metamorphic overprint (Yang and Shau, 1988; Chen et al., submitted). Zircon grains yielded a youngest age of 24

Ma, consistent with the strata age (Chen et al., submitted). Neighboring strata strike northeast and dip moderately to the southeast. Cleavage in adjacent slate has similar attitudes as the beddings but with steeper dips. The cleavage within the pyroclastics is spaced and not penetrative as is the case in the adjacent slates. On those ~1 cm-apart pressure solution planes, numerous mm-scale muscovite porphyroblasts containing chloritic minerals or albite are found along and parallel to the foliation, demonstrating their syn-kinematic origin (Fig. 2A and B). Deformation of the pyroclastics and the entire Hsuehshan Range rocks was dominated by pure shear (Fig. 2; Clark et al., 1993; Tillman and Byrne, 1995; Fisher et al., 2002). Maximum burial temperature of about 250 °C was constrained by nearby (slate sample NCIH-12; Fig. 1B) Raman spectroscopy of carbonaceous material (RSCM) data (246 ± 5 °C; Chen et al., submitted), similar to those obtained by vitrinite reflectance data (<300 °C; Chen et al., 2011) and the metamorphic petrology of the pyroclastics (~220 °C; Shau and Yang, 1987), and is far lower than the closure temperature for K-Ar system of muscovite (~490 °C for grain half-size at 500 μm under a cooling rate of 10 °C/Myr; Harrison et al., 2009). This relationship where large synkinematic micas grow at low temperature conditions offers a rare opportunity to date cleavage directly (Chan et al., 2000), a task not yet achieved in the Taiwan Orogen. The retrograde cooling can be deduced from the apatite fission-track result of a nearby meta-

sandstone, which is 1.6 ± 0.3 Ma (Wang, 2011) consistent with orogen-wide rapid exhumation (Lee et al., 2015).

3. In-situ $^{40}Ar/^{39}Ar$ laser microprobe dating

3.1. Sample description

In order to date the mineral fabrics of the mica porphyroblasts of the NCIH-B2 sample, a thick section of approximately 2 mm thick and 1 cm² in area containing one major pressure solution seam was cut perpendicular to the spaced pressure solution cleavage (Fig. 2C) and prepared following Chan et al. (2000) for in-situ $^{40}Ar/^{39}Ar$ laser microprobe dating. At least three mica porphyroblasts are present along the seam and are composed of muscovite with minor corrensite, a potassium-bearing chloritic mineral usually formed by alteration of basic igneous rocks (Shau et al., 1990). Both minerals are not primary grains within the host Sule Bridge Pyroclastics: corrensite may be directly derived from alteration of the mafic minerals in the pyroclastics (Furbish, 1975; Evarts and Schiffman, 1983), while muscovite is likely originated from neighboring sedimentary strata due to the mafic content of the pyroclastics. Grains of the two minerals are stacked and intercalated parallel to the foliation demonstrating the syn-kinematic and co-genetic nature of their growth with the pressure solution foliation. As demonstrated by the shapes and texture of the mica porphyroblasts as well as features around the pressure solution seams (Fig. 2), formation of foliation within the NCIH-B2 sample was generally through pure-shear deformation. Further constraints on the metamorphic condition when the mica porphyroblasts and the host pressure solution seams formed can be derived from the overlapping stability fields of the two concomitant minerals: corrensite is found to be stable below ~250 °C in hydrothermal systems (Cathelineau and Izquierdo, 1988), while enduring muscovite presence emerging from illite is higher than ~250 °C as the high anchizone (Merriman and Peacor, 1999). This implies the formation condition of the host foliation and the porphyroblasts is rather constantly at ~250 °C, coinciding with the maximum temperature inferred by the RSCM data from nearby slate (246 ± 5 °C; Chen et al., submitted). Both the estimated porphyroblast growth temperature (~250 °C) and peak metamorphic temperature of the sample (246 ± 5 °C) was markedly lower than the K-Ar resetting temperature of muscovite (~490 °C) as previously noted.

3.2. $^{40}Ar/^{39}Ar$ methodology

Isotopic composition of Ar gases is extracted by using in-situ $^{40}Ar/^{39}Ar$ laser microprobe analyses which create pits of tens of microns, allowing high spatial resolution of ages within the mica porphyroclasts. The thick section of NCIH-B2 sample cut normal to foliation was first polished and rinsed by acetone and distilled water. Before neutron irradiation, the polished chip was imaged by scanning electron microscope (FEI QUANTA 200F field emission scanning electron microscope, housed in the Geosciences Department, National Taiwan University) with mineral chemical compositions quantitatively analyzed by energy dispersive spectrometer (coupled with the SEM). Along with flux monitor (LP-6 biotite; Odin, 1982), the sample was wrapped in aluminum foil and irradiated in the VT-C position at the Tsing-Hua Open-Pool Reactor (THOR), Taiwan, for 16 h, with a fast neutron flux of 1.566 × 10¹³ n (cm²s)⁻¹. J value (0.00326220 ± 0.00001077 at 1-sigma level) was calculated from the argon composition released from the LP-6 biotite monitor with a calibrated $^{40}Ar/^{39}Ar$ age of 128.5 ± 0.5 Ma based on Fish Canyon Sanidine (28.305 ± 0.036 Ma; Renne et al., 2010). After irradiation, samples were loaded into an ultra-high-vacuum laser port and baked to 200 °C overnight using a heat

oven to remove atmospheric contamination.

In-situ $^{40}Ar/^{39}Ar$ laser microprobe analysis was carried out using a New Wave LUV 266 laser ablation system. Laser ablation was performed using 20 W laser focused as 10 μm in size for 3 min which results in a crater of a few tens of μm in diameter, and 4 to 6 sites were ablated together for optimal signal detection due to the young ages of the targeted mica porphyroblasts. Gas was collected and purified for 2 min using two getters (one was kept at 450 °C and the other at room temperature) to remove active gases (e.g., CO_2, H_2O, CH_4, etc.).

Argon isotopic measurements of the purified gas were made on a fully automated, high-resolution Nu-Instruments Noblesse multi-collector mass spectrometer at National Taiwan University. Peak intensities were extrapolated back to the inlet time by linear regression, and then data were corrected for system blanks, mass spectrometer discrimination, isotopic decay and neutron-induced interference reactions. The interference factors, $(^{39}Ar/^{37}Ar)$ Ca = 0.00065 ± 0.000047, $(^{36}Ar/^{37}Ar)$Ca = 0.000255 ± 0.000028 and $(^{40}Ar/^{39}Ar)$K = 0.0287 ± 0.01722, were obtained by analyzing irradiated calcium and potassium salts. Detailed analytical procedures and data processing methods are similar to those given by Lo et al. (2002).

3.3. Results

We performed 120 and 5 laser microprobe analyses on muscovite and corrensite grains, respectively (Fig. 3A). The results are presented in Fig. 3B with the obtained age of each analysis marked on the probed site. The error of each analysis falls between 0.3 and 1.5 Ma with most around 0.6 Ma. Diffusion does not pose significant effects to the results considering the mm-scale mineral grain sizes as well as the well-defined thermal history. Ages from muscovite fabrics are distributed over a rather long time span, from 6.2 to 2.3 Ma with a mean age of 4.6 Ma; ages from corrensite fabrics are also dispersed between 2.5 and 5 Ma (Fig. 3C). All dates are within the proposed time window of the Taiwan Orogeny (latest Miocene to present; Teng, 1990; Lo and Onstott, 1995; Lin et al., 2003; Huang et al., 2006), confirming that these mica porphyroblasts were syn-kinematic newly-grown products of the Neogene mountain building processes. The detailed results of the in-situ $^{40}Ar/^{39}Ar$ laser microprobe analysis are listed in Table 1.

The spatial distribution of the ages within the mica porphyroblasts, unlike what commonly expected in strain fringe microstructures (e.g. Passchier and Trouw, 2005), does not follow any radial or linear trends (Fig. 3B). Both along-fiber (Fig. 4A) and cross-fiber (Fig. 4B) variations of obtained ages are seemingly random, and contain numerous discontinuities even after taking into account of the error of each analysis. This indicates the development of dated mica porphyroblasts was neither continuous nor uniform, but with frequent hiatuses and changes in locations of new-growth.

4. Formation condition of the Taiwanese mica porphyroblasts

The mica porphyroblast growth ages, together with constraints from zircon U-Pb dates, RSCM, metamorphic mineral assemblage and apatite fission-track date, constitute a complete time-temperature history for the NCIH-B2 sample (Chen et al., submitted), the first such record achieved in Taiwan. The mafic pyroclastics was formed no earlier than 24 Ma, as told by the youngest dated U-Pb zircon crystallization age, within the latest-Oligocene Tatungshan Formation. This Sule Bridge pyroclastics resided within the continental margin until late Miocene as suggested by the age of the topmost strata in the Sule Formation (Teng, 1992), the youngest passive margin deposits in the northern Hsuehshan Range, and up to 2 km in depth estimated by the
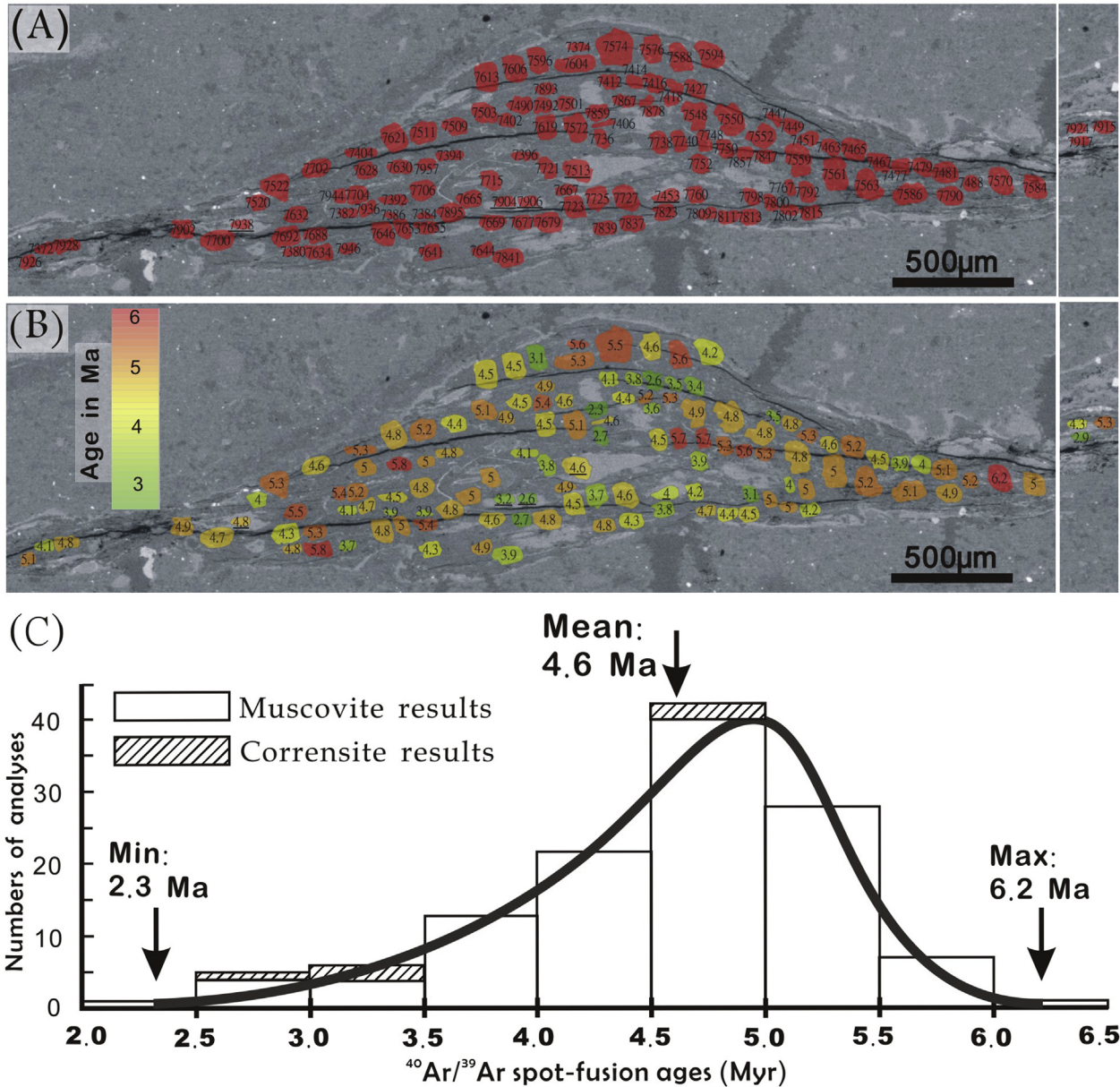
Fig. 3. A: Numbered $^{40}Ar/^{39}Ar$ laser microprobe dating sites over the BSE image, with the analyses on corrensite fabrics underlined. B: The $^{40}Ar/^{39}Ar$ laser microprobe dating sites marked with and color-coded according to the obtained ages over the BSE image; corrensite results underlined. C: Histogram of the $^{40}Ar/^{39}Ar$ laser microprobe ages.

thickness of margin sediments above. Immediately followed was the rapid underthrusting of the margin sedimentary succession containing the NCIH-B2 body beneath the pro-wedge part of the Taiwan orogenic wedge, a process that brought in dynamic metamorphism that overprinted burial diagenesis (Chen et al., 2011). The peak condition that the Sule Bridge Pyroclastics suffered during the underthrusting was ~250 °C determined by RSCM data (246 ± 5 °C) from a neighboring slate, equivalent to ~8 km depth assuming a simplified linear 30 °C/km geotherm. The muscovite-corrensite mineral assemblage of the dated mica porphyroblasts which are co-genetic with the host pressure-solution seam dictates that the porphyroblasts were grown exactly at the peak state (section 3.1). Thus the analyzed mica porphyroblasts and the foliation they reside in developed persistently between 6.2 and 2.3 Ma. After staying at ~250 °C for nearly 4 Myrs, the NCIH-B2 body underwent fast cooling and exhumation as the local apatite fission-track constraint, ~1.6 Ma at ~140 °C (Wang, 2011), indicates an

uplift rate around 3 mm/yr for both 2.3–1.6 Ma and 1.6 Ma to present (Chen et al., submitted). Prolonged peak state residence with continued deformation following rapid prograde heating and before fast exhumation characterizes the thermal evolution of the northern Hsuehshan Range rocks as revealed by the NCIH-B2 sample.

The time-temperature-depth history documented from the Sule Bridge Pyroclastics is best appreciated in light of orogenic wedge kinematics. Basal accretion is considered as a major mechanism contributing material influx into the Taiwanese orogenic wedge (Fuller et al., 2006; Beyssac et al., 2007), and the Hsuehshan Range on the pro-wedge side of the mountain belt is one of the tectonic underplating sites (Simoes et al., 2007; Malavieille, 2010). The underplated units in the Hsuehshan Range are only outcropping in its northern part (Chen et al., 2011) since the north experienced relatively more denudation and rock uplift than the south due to the special time-space relationship of the Taiwan orogeny (Teng,

Table 1
Results of *in-situ* $^{40}Ar/^{39}Ar$ laser microprobe dating on sample NCIH-B2.

Analysis no.	$^{40}Ar/^{39}Ar \pm \sigma$	$^{37}Ar/^{39}Ar \pm \sigma$	$^{36}Ar/^{39}Ar \pm \sigma$	Age $\pm 2\sigma$
Results of *in-situ* $^{40}Ar/^{39}Ar$ laser microprobe dating on muscovite sites of sample NCIH-B2				
7372	1.511793 ± 0.009991	0.026721 ± 0.002337	0.002816 ± 0.000237	4.13 ± 0.90
7374	1.487040 ± 0.013288	0.020462 ± 0.004627	0.001937 ± 0.000318	5.60 ± 1.20
7380	1.507192 ± 0.010686	0.034432 ± 0.004445	0.002416 ± 0.000131	4.84 ± 0.53
7382	1.641386 ± 0.014862	0.033765 ± 0.003178	0.003248 ± 0.000210	4.14 ± 0.81
7384	1.837395 ± 0.013460	0.013764 ± 0.002521	0.004025 ± 0.000228	3.92 ± 0.87
7386	1.878313 ± 0.013432	0.024977 ± 0.001013	0.004153 ± 0.000147	3.94 ± 0.59
7392	1.526965 ± 0.011443	0.032877 ± 0.002356	0.002657 ± 0.000162	4.52 ± 0.64
7394	1.641985 ± 0.011114	0.017183 ± 0.001779	0.002887 ± 0.000081	4.80 ± 0.37
7396	1.578144 ± 0.012446	0.022772 ± 0.002924	0.003067 ± 0.000226	4.08 ± 0.86
7402	1.487665 ± 0.009158	0.020552 ± 0.002205	0.002328 ± 0.000113	4.88 ± 0.47
7404	1.657207 ± 0.011923	0.030810 ± 0.002912	0.002694 ± 0.000216	5.26 ± 0.83
7406	1.779471 ± 0.012836	0.024254 ± 0.002591	0.003463 ± 0.000155	4.59 ± 0.62
7412	1.692429 ± 0.012730	0.028523 ± 0.002412	0.003455 ± 0.000120	4.07 ± 0.50
7414	1.735516 ± 0.012551	0.022701 ± 0.002039	0.003755 ± 0.000118	3.79 ± 0.49
7416	2.043748 ± 0.012434	0.019600 ± 0.001140	0.005421 ± 0.000160	2.63 ± 0.62
7418	1.771465 ± 0.013473	0.030561 ± 0.002958	0.004060 ± 0.000166	3.45 ± 0.66
7427	1.958107 ± 0.011659	0.025277 ± 0.001415	0.004725 ± 0.000144	3.38 ± 0.57
7447	1.891940 ± 0.011709	0.019920 ± 0.001097	0.004423 ± 0.000151	3.52 ± 0.59
7449	1.767332 ± 0.013300	0.035163 ± 0.001519	0.003303 ± 0.000158	4.82 ± 0.63
7451	1.643745 ± 0.016969	0.030392 ± 0.002069	0.002616 ± 0.000149	5.32 ± 0.61
7463	1.593801 ± 0.009335	0.024874 ± 0.001907	0.002849 ± 0.000122	4.58 ± 0.50
7465	1.541032 ± 0.010926	0.023095 ± 0.002238	0.002359 ± 0.000093	5.15 ± 0.41
7467	1.496406 ± 0.011146	0.024003 ± 0.002154	0.002569 ± 0.000145	4.49 ± 0.58
7477	1.797404 ± 0.011657	0.037464 ± 0.002530	0.003894 ± 0.000228	3.92 ± 0.87
7479	1.590298 ± 0.010668	0.027606 ± 0.002130	0.003145 ± 0.000093	4.01 ± 0.40
7481	1.618253 ± 0.010240	0.027441 ± 0.001604	0.002671 ± 0.000211	5.06 ± 0.81
7488	1.556830 ± 0.011677	0.028604 ± 0.001650	0.002416 ± 0.000114	5.15 ± 0.48
7490	1.601309 ± 0.012368	0.023054 ± 0.002964	0.002908 ± 0.000155	4.52 ± 0.62
7492	1.559094 ± 0.011111	0.022324 ± 0.001868	0.002267 ± 0.000129	5.43 ± 0.53
7501	1.892655 ± 0.013302	0.030339 ± 0.005601	0.003838 ± 0.000171	4.61 ± 0.67
7503	1.508861 ± 0.008920	0.032168 ± 0.002146	0.002264 ± 0.000156	5.13 ± 0.62
7509	1.601158 ± 0.010444	0.025381 ± 0.002793	0.002992 ± 0.000108	4.36 ± 0.45
7511	1.507802 ± 0.011613	0.029422 ± 0.001367	0.002226 ± 0.000168	5.20 ± 0.66
7520	1.568974 ± 0.010038	0.023923 ± 0.001903	0.003062 ± 0.000106	4.03 ± 0.45
7522	1.449722 ± 0.008197	0.023018 ± 0.001829	0.001980 ± 0.000208	5.28 ± 0.80
7548	1.726123 ± 0.011736	0.022703 ± 0.001489	0.003115 ± 0.000087	4.91 ± 0.39
7550	1.627233 ± 0.011487	0.025123 ± 0.001315	0.002828 ± 0.000100	4.82 ± 0.44
7552	1.498268 ± 0.008737	0.024955 ± 0.001082	0.002414 ± 0.000128	4.79 ± 0.52
7559	1.619795 ± 0.012124	0.023144 ± 0.002124	0.002801 ± 0.000089	4.83 ± 0.40
7561	1.552971 ± 0.011165	0.023251 ± 0.001386	0.002505 ± 0.000104	4.96 ± 0.44
7563	1.439619 ± 0.009548	0.029802 ± 0.002068	0.001995 ± 0.000074	5.20 ± 0.35
7570	1.560566 ± 0.014398	0.028579 ± 0.002812	0.001842 ± 0.000161	6.23 ± 0.65
7572	1.554269 ± 0.010540	0.029519 ± 0.001728	0.002454 ± 0.000130	5.06 ± 0.53
7574	1.406144 ± 0.009446	0.030303 ± 0.001329	0.001740 ± 0.000121	5.46 ± 0.50
7576	1.431768 ± 0.011250	0.024775 ± 0.002167	0.002299 ± 0.000115	4.59 ± 0.49
7584	1.473383 ± 0.009468	0.022935 ± 0.001708	0.002228 ± 0.000150	4.97 ± 0.60
7586	1.477426 ± 0.009753	0.026798 ± 0.002633	0.002199 ± 0.000111	5.06 ± 0.47
7588	1.433170 ± 0.011182	0.025613 ± 0.002161	0.001739 ± 0.000224	5.63 ± 0.86
7594	2.114389 ± 0.012617	0.023231 ± 0.001241	0.004780 ± 0.000216	4.24 ± 0.82
7596	1.544618 ± 0.009355	0.023876 ± 0.002501	0.003477 ± 0.000238	3.12 ± 0.90
7604	1.564045 ± 0.011416	0.029027 ± 0.003222	0.002369 ± 0.000127	5.28 ± 0.52
7606	1.513918 ± 0.009060	0.024156 ± 0.002044	0.002647 ± 0.000095	4.46 ± 0.41
7613	1.447148 ± 0.009580	0.029853 ± 0.001332	0.002414 ± 0.000136	4.48 ± 0.55
7619	1.530936 ± 0.011197	0.027589 ± 0.001573	0.002663 ± 0.000076	4.53 ± 0.36
7621	1.531807 ± 0.008602	0.029729 ± 0.001948	0.002520 ± 0.000121	4.80 ± 0.50
7628	1.444572 ± 0.009256	0.022667 ± 0.001818	0.002104 ± 0.000098	5.02 ± 0.42
7630	1.660985 ± 0.012195	0.025542 ± 0.002083	0.002415 ± 0.000167	5.79 ± 0.66
7632	1.479322 ± 0.010436	0.024444 ± 0.003818	0.001980 ± 0.000158	5.47 ± 0.63
7634	1.649263 ± 0.012418	0.025226 ± 0.002568	0.002397 ± 0.000149	5.75 ± 0.60
7641	1.586238 ± 0.011456	0.031015 ± 0.001681	0.002991 ± 0.000264	4.27 ± 0.99
7644	1.759785 ± 0.013483	0.024915 ± 0.002120	0.003229 ± 0.000139	4.91 ± 0.56
7646	1.556125 ± 0.011947	0.020635 ± 0.002817	0.002602 ± 0.000147	4.80 ± 0.59
7653	1.554884 ± 0.009376	0.032066 ± 0.003088	0.002475 ± 0.000145	5.03 ± 0.58
7655	1.553475 ± 0.008836	0.026866 ± 0.002686	0.002290 ± 0.000215	5.36 ± 0.82
7665	1.596544 ± 0.011336	0.033643 ± 0.001661	0.002649 ± 0.000146	4.97 ± 0.58
7667	1.693199 ± 0.014992	0.020593 ± 0.001887	0.003009 ± 0.000146	4.90 ± 0.59
7669	1.565593 ± 0.009717	0.025827 ± 0.002412	0.002724 ± 0.000249	4.63 ± 0.94
7677	1.583010 ± 0.011849	0.026681 ± 0.002394	0.003840 ± 0.000185	2.69 ± 0.71
7679	1.667048 ± 0.012458	0.019702 ± 0.004286	0.003000 ± 0.000349	4.75 ± 1.31
7688	1.616942 ± 0.011844	0.030459 ± 0.004465	0.002547 ± 0.000245	5.28 ± 0.93
7692	1.569387 ± 0.008464	0.029863 ± 0.003625	0.002902 ± 0.000177	4.33 ± 0.69
7700	1.441665 ± 0.010297	0.026296 ± 0.003312	0.002288 ± 0.000187	4.67 ± 0.72
7702	1.611266 ± 0.012696	0.027538 ± 0.003243	0.002893 ± 0.000152	4.61 ± 0.61

Table 1 (*continued*)

Analysis no.	$^{40}Ar/^{39}Ar \pm \sigma$	$^{37}Ar/^{39}Ar \pm \sigma$	$^{36}Ar/^{39}Ar \pm \sigma$	Age $\pm 2\sigma$
7704	1.686018 ± 0.012193	0.013334 ± 0.002746	0.002820 ± 0.000239	5.20 ± 0.91
7706	1.497694 ± 0.010816	0.030634 ± 0.004188	0.002403 ± 0.000166	4.81 ± 0.65
7715	1.558099 ± 0.010991	0.026221 ± 0.003915	0.002477 ± 0.000292	5.04 ± 1.10
7721	1.664341 ± 0.010362	0.028753 ± 0.003886	0.003494 ± 0.000214	3.83 ± 0.82
7723	1.766261 ± 0.011619	0.030901 ± 0.002368	0.003478 ± 0.000214	4.49 ± 0.81
7725	1.867604 ± 0.014364	0.015119 ± 0.001896	0.004252 ± 0.000359	3.69 ± 1.34
7727	1.675111 ± 0.011967	0.026115 ± 0.003288	0.003135 ± 0.000128	4.56 ± 0.52
7736	1.650135 ± 0.010053	0.031132 ± 0.002266	0.004077 ± 0.000275	2.67 ± 1.03
7738	1.702610 ± 0.012561	0.027986 ± 0.005091	0.003277 ± 0.000184	4.47 ± 0.71
7740	1.715165 ± 0.010945	0.029502 ± 0.002066	0.002648 ± 0.000285	5.70 ± 1.07
7748	1.593136 ± 0.011467	0.031650 ± 0.002976	0.002245 ± 0.000176	5.69 ± 0.69
7750	1.649529 ± 0.012463	0.023058 ± 0.003048	0.002638 ± 0.000285	5.31 ± 1.07
7752	1.679126 ± 0.012763	0.026669 ± 0.002759	0.003496 ± 0.000159	3.92 ± 0.63
7760	1.714346 ± 0.012522	0.015530 ± 0.003529	0.003462 ± 0.000139	4.19 ± 0.56
7767	1.544106 ± 0.012162	0.021643 ± 0.004055	0.003002 ± 0.000359	3.99 ± 1.34
7790	1.633746 ± 0.012307	0.028688 ± 0.002012	0.002823 ± 0.000260	4.88 ± 0.98
7792	1.580454 ± 0.012511	0.033989 ± 0.002495	0.002599 ± 0.000163	4.96 ± 0.64
7798	1.607800 ± 0.011026	0.023071 ± 0.002621	0.003702 ± 0.000226	3.10 ± 0.86
7800	1.614013 ± 0.011555	0.017918 ± 0.004208	0.002692 ± 0.000188	4.99 ± 0.73
7802	1.843719 ± 0.012390	0.020334 ± 0.002272	0.003464 ± 0.000162	4.99 ± 0.64
7809	1.746450 ± 0.011263	0.022597 ± 0.002532	0.003317 ± 0.000195	4.66 ± 0.75
7811	1.677451 ± 0.011268	0.021091 ± 0.001822	0.003250 ± 0.000184	4.36 ± 0.71
7813	1.666727 ± 0.010617	0.022327 ± 0.001663	0.003142 ± 0.000155	4.49 ± 0.61
7815	1.840968 ± 0.014003	0.020605 ± 0.003092	0.003881 ± 0.000155	4.21 ± 0.62
7823	1.697608 ± 0.011567	0.026751 ± 0.001958	0.003687 ± 0.000175	3.84 ± 0.65
7837	1.795725 ± 0.011184	0.027419 ± 0.001637	0.003755 ± 0.000176	4.32 ± 0.65
7839	1.845669 ± 0.012567	0.025138 ± 0.004439	0.003648 ± 0.000240	4.83 ± 0.88
7841	1.864921 ± 0.011955	0.010557 ± 0.002117	0.004236 ± 0.000353	3.86 ± 1.30
7847	1.670587 ± 0.011687	0.028296 ± 0.001652	0.002829 ± 0.000294	5.25 ± 1.08
7857	1.640687 ± 0.010376	0.030592 ± 0.005003	0.002568 ± 0.000114	5.55 ± 0.43
7859	1.961359 ± 0.015424	0.038603 ± 0.006039	0.005399 ± 0.000337	2.33 ± 1.24
7867	1.809163 ± 0.012332	0.027641 ± 0.005200	0.003736 ± 0.000300	4.44 ± 1.11
7876	1.788204 ± 0.010551	0.020340 ± 0.003900	0.003229 ± 0.000225	5.24 ± 0.83
7878	1.756664 ± 0.010966	0.024391 ± 0.005270	0.004032 ± 0.000271	3.57 ± 1.00
7891	1.808957 ± 0.012824	0.010951 ± 0.004296	0.003291 ± 0.000286	5.25 ± 1.05
7893	1.849140 ± 0.012775	0.020608 ± 0.004690	0.003617 ± 0.000275	4.90 ± 1.01
7895	1.753563 ± 0.011197	0.020608 ± 0.001548	0.003364 ± 0.000125	4.78 ± 0.46
7902	1.764146 ± 0.013527	0.026475 ± 0.006029	0.003327 ± 0.000388	4.91 ± 1.43
7915	1.740845 ± 0.012275	0.023250 ± 0.004667	0.003016 ± 0.000272	5.34 ± 1.00
7917	1.936685 ± 0.014633	0.016599 ± 0.004822	0.005000 ± 0.000240	2.90 ± 0.88
7924	1.869883 ± 0.015694	0.014494 ± 0.005066	0.003991 ± 0.000348	4.34 ± 1.28
7926	1.731211 ± 0.012628	0.026699 ± 0.004144	0.003136 ± 0.000259	5.06 ± 0.95
7928	1.617155 ± 0.014299	0.035263 ± 0.004352	0.002891 ± 0.000312	4.81 ± 1.15
7936	1.419025 ± 0.012924	0.039296 ± 0.004640	0.002313 ± 0.000368	4.65 ± 1.36
7944	1.660928 ± 0.014177	0.026857 ± 0.005356	0.002695 ± 0.000352	5.44 ± 1.30
7946	1.727549 ± 0.013357	0.037427 ± 0.005745	0.003845 ± 0.000244	3.74 ± 0.90
7957	1.643964 ± 0.010770	0.030654 ± 0.002437	0.002899 ± 0.000219	4.96 ± 0.81
Results of $^{40}Ar/^{39}Ar$ *in-situ* laser microprobe dating on corrensite sites of sample NCIH-B2				
7513	1.735678 ± 0.010763	0.025232 ± 0.002523	0.003310 ± 0.000169	4.61 ± 0.66
7602	2.204258 ± 0.014750	0.017311 ± 0.004189	0.005543 ± 0.000199	3.39 ± 0.76
7904	1.790614 ± 0.020013	0.011200 ± 0.004381	0.004373 ± 0.000400	3.15 ± 1.48
7906	2.112276 ± 0.012936	0.014119 ± 0.005766	0.005741 ± 0.000323	2.62 ± 1.19
7938	1.839734 ± 0.012903	0.026136 ± 0.005389	0.003634 ± 0.000312	4.82 ± 1.15

1990). The rapid underthrusting and resultant prograde heating following basin burial as delineated in the thermal history of the NCIH-B2 body are products of the basal accretion process (Glodny et al., 2005). The earliest obtained porphyroblast growth age, 6.2 Ma, is close to the onset of the mountain building for northern to central Taiwan (Lin et al., 2003). Therefore, basal accretion has been operating since the beginning stages of the Taiwan mountain building. The northern Hsuehshan Range units containing the Sule Bridge Pyroclastics continued to deform during the following 4 Myrs at temperatures around 250 °C when rapid convergence and associated underplating persisted, marking a period of significant downward thickening of the orogenic wedge in the Hsuehshan Range vicinity (Chen et al., submitted; Chen et al., 2016).

5. Implications for the growth mechanisms of mica fish

While the extended time range of *in-situ* $^{40}Ar/^{39}Ar$ laser microprobe ages may be attributed to the protracted residence at the peak metamorphic state, the apparently irregular spatial distribution of the ages (Figs. 3 and 4) reveals the possible mechanisms responsible for the growth and deformation of the dated mica porphyroblasts. Their lensoid shape and foliation-parallel long axis resemble mica fish albeit in a lower metamorphic grade. Based on mineralogical and structural characteristics, internal slips on crystallographic cleavage, grain rotation, and bending of fabrics during simple shear are considered the main mechanisms of mica fish genesis (ten Grotenhuis et al., 2003; Mukherjee, 2011, Fig. 5A); some geochronological and geochemical analyses have found that, on the other hand, peripheral syn-kinematic recrystallization and precipitation constitute a key integral part in the formation of mica fish (e.g. Mulch et al., 2005, Fig. 5B). The first theory of simple-shear grain deformation plus grain rotation is not the primary mechanisms for the dated fish-like porphyroblasts reported herein, because they were neither pre-existing porphyroclasts of the
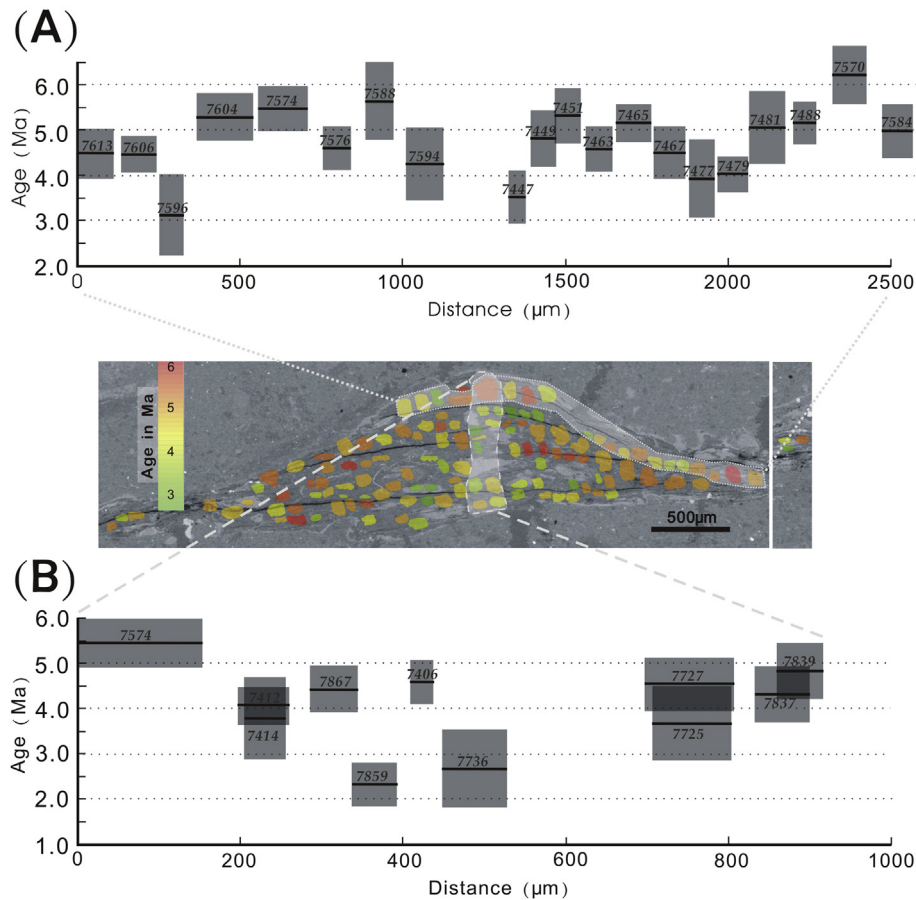
Fig. 4. A: Selected $^{40}Ar/^{39}Ar$ laser microprobe ages demonstrating fabric-parallel variations, with inset BSE map showing the selected sites. B: Selected $^{40}Ar/^{39}Ar$ laser microprobe ages demonstrating cross-fabric variations, with inset BSE map showing the selected sites.

pyroclastics (muscovite and corrensite were not constituents in the mafic protolith of the Sule Bridge Pyroclastics; Shau and Yang, 1987) but syn-kinematic new growth during the Neogene orogeny, nor controlled by simple-shear deformation as pure-shear was dominant (Fig. 2). The mica porphyroblasts investigated do not possess overall outward-decreasing age trends as observed in Mulch et al. (2005), suggesting the second theory involving syntaxial growth in strain fringes was again not chiefly responsible. While no along-fiber variations are visible under the BSE image (Fig. 2C), abrupt changes are common in the obtained $^{40}Ar/^{39}Ar$ laser microprobe ages (Fig. 4) while significant Ar diffusion is not expected. The growth of grains within the porphyroblasts was therefore often punctuated, and following new growths can be located at the ends or in the middle of existing grains.

Considering the pure-shear deformation responsible for the formation of the NCIH-B2 mica porphyroblasts and the host pressure solution seam, with generally grain-normal contraction and grain-parallel extension consistent with the quartz veinlets, we propose that the spatial age pattern resembles a boudinage process with new-growths at the crack-seal sites as well as at the lateral strain fringes. Material supply for porphyroblast growth was plentiful because metamorphic fluid originated from neighboring slate circulated through the pressure solution seam allowing muscovite to precipitate. Similarly, corrensite of mafic mineral alterations within the pyroclastic body was readily driven to the cleavage seam during the pressure solution process. For example, in the along-fiber age variation shown in Fig. 4A the muscovite fabrics in areas of analyses 7604, 7574, and 7588 were precipitated at ~5.5 Ma, which were followed by new precipitations on the left tip

(areas of analyses 7613 and 7606) and right tip (area of analysis 7594) as well as in the middle (area of analysis 7576) at ~4.5 Ma, and another precipitation at ~3 Ma again in the middle of the fabrics (area of analysis 7596); the two intra-grain growths were records of boudinage events that the voids between extensional boudins were created ("crack") and sealed at ~ 4.5 and ~3 Ma. Between 2.5 and 5 Ma the circulating fluid sometimes contained abundant corrensite solute which was also precipitated in the mica porphyroblast though of much lesser volume; the resultant corrensite grains often show signs of foliation-normal contraction and may serve as border markers of some micro-boudins (Fig. 2C). Besides, light-colored hairlines of probable corrensite composition often at high angles to mica grains inside the porphyroblast (Fig. 2C) may also be relics of crack-seal events with minute void openings, and their curved shapes resulted from porphyroblast internal deformation. Throughout the boudinage-filling history the lateral continuity of the mica crystals were preserved with mineral cleavage parallel to the foliation and the porphyroblast bodies. The crack-seal process deduced here is different from the chlorite-muscovite aggregates reported in Clark and Fisher (1995) and biotite-chlorite porphyroblasts in Barker (2002), in which existing porphyroclasts aligned at high angle to foliation were cracked along mineral cleavage planes and new-growths were foliation-parallel, creating domains of contrasting crystal orientations (Fig. 5C).

To illustrate how the proposed boudinage process took place in the development of the analyzed mica porphyroblasts, the fibers of the central porphyroblast were tentatively assigned to pre-5 Ma, 4-5 Ma, and post-4 Ma areas that are indicated by the laser microprobe ages (Fig. 6A). Mica porphyroblast reconstructions were
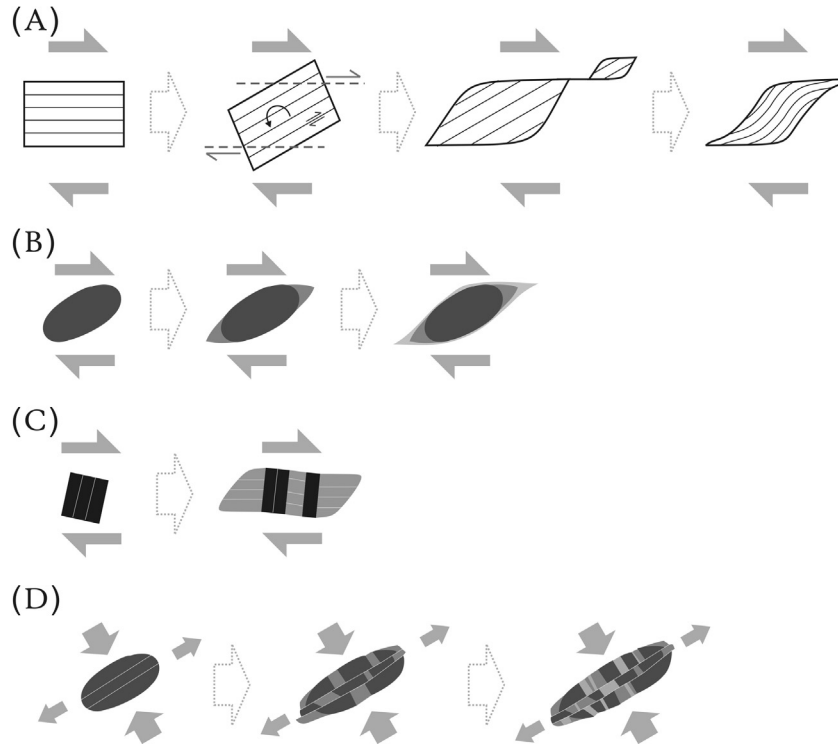
Fig. 5. Models of mica fish/porphyroblast development. A: Formation through grain rotation, bending and shear slips on preferred crystallographic planes with minor size reduction (after ten Grotenhuis et al., 2003); B: Syn-kinematic growth of new mica fiber along the rim and at tips of strain shadow; C: Crack-fill mica porphyroblastesis with contrasting mineral orientation domains (after Barker, 2002); D: Boudin-style growth of mica fish/porphyroblast dominated by crack-seal mechanism with laterally continuous mica grains as proposed in this study.
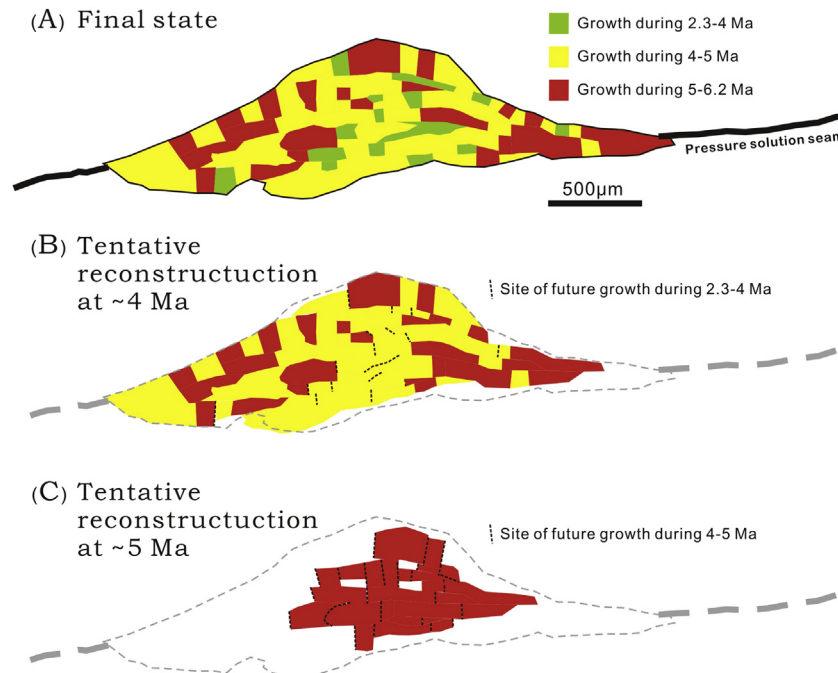
Fig. 6. Schematic growth history of the analyzed mica porphyroblast. A: the final state of the porphyroblast with fabrics loosely ascribed to the 6.2-5, 5-4, and 4-2.3 Ma intervals according to the obtained laser microprobe ages. B: Tentative reconstruction of the analyzed porphyroblast at ~4 Ma with sites of later growth (4–2.3 Ma) marked. C: same as B at ~5 Ma. Most deformation in the reconstructions of B and C involved brittle necking of the fibers and fabric-parallel (sub-) grain sliding.

attempted at ~4 and ~5 Ma by closing the spaces of later growths through mostly along-fabric sliding (Fig. 6B and C). Between 4 and 5 Ma when the mica porphyroblast was fast growing, some new

fibers were deposited at lateral edges of pre-existing sub-grains, while more precipitations occurred within former fabrics as void sealing of boudinage cracks (Fig. 6B). All the post-4 Ma

precipitations were in the interior of the porphyroblast body and were infill of boudin gaps (Fig. 6C). The extension directions deduced by the reconstructions were generally foliation-parallel, consistent with the flattening direction of the overall pure shear deformation. Boudins seem to be restricted within individual sub-grains as no simultaneous straight crack filling across the entire porphyroblast was found, and those sliding mineral cleavage planes may have served as mechanical barriers.

The boudinage structure is exclusively within the mica porphyroblasts as no direct correlations between micro-boudin cracks and the quartz veins in neighboring rock matrix could be found, and those quartz veinlets failed to cut across the mica porphyroblasts (Fig. 2). Contrast in rheology may be responsible: the rock matrix surrounding the analyzed mica porphyroblasts has undergone extensive metasomatism to a mixture of very fine-grained quartz, calcite and chlorite grains, while the mica porphyroblasts consist of mm-scale brittle mica crystals aligned to rock foliation. The porphyroblast-matrix contact may act as mechanical barrier that the mica grains within were prone to brittle fracturing under lateral stretching, but the rock matrix outside behaved more ductile or was relatively stronger to tensile cracking.

The brittle boudinage process through crack-seal with associated mineral cleavage slips deduced for the development of fish-like mica porphyroblasts from the Sule Bridge Pyroclastics is markedly different from existing documentations (e.g. ten Grotenhuis et al., 2003; Mulch et al., 2005; Barker, 2002). A key factor may be the contrasting formation conditions as the present case took place at brittle-ductile transition depths around 8 km deep, while the majority of studied fish and porphyroblasts were grown under high-grade mylonitic states (Passchier and Trouw, 2005). However, the low-temperature peak metamorphism during pure-shear deformation in the NCIH-B2 sample allowed the preservation of incremental growth records in the K-Ar radioisotope system which is otherwise lost by thermal resetting for mica fish in high-temperature rocks. We thus propose that tensile crack-seal syntaxial growth can be considered as one of the mica fish development mechanisms (Fig. 5D), especially for cases within low-grade metamorphic rocks.

6. Concluding remarks

Mica porphyroblasts from the northern Hsuehshan Range of Taiwan in the mafic Sule Bridge Pyroclastics were analyzed by using in-situ ^{40}Ar/^{39}Ar laser microprobe to document their age distribution and potential growth mechanism under low-grade metamorphism. The mica porphyroblasts grew syn-kinematically within the mafic host rock that shows pressure solution deformation at temperatures around 250 °C, a condition well below the closure temperature for the K-Ar system in muscovite. The dating results thus illustrate formation ages of the mica porphyroblasts and show a protracted growth history from ~6 to ~2.5 Ma. The temporal distribution of ages indicates that the deformation and growth of mica porphyroblasts starting from the onset of arc-continent collision in Taiwan and ending prior to the rapid cooling and exhumation in the later stages of the Taiwan orogeny. The spatial distribution of the ages within the mica porphyroblasts reveals variable age domains and the domain patterns are consistent with the crack-seal growth of the mica porphyroblasts.

References

Barker, A.J., 2002. Crack-fill prophyroblastesis. J. Metamorph. Geol. 20, 283–294.

Beyssac, O., Simoes, M., Avouac, J.-P., Farley, K.A., Chen, Y.-G., Chan, Y.-C., Goffe, B., 2007. Late Cenozoic metamorphic evolution and exhumation of Taiwan. Tectonics 26, TC6001.

Cathelineau, M., Izquierdo, G., 1988. Temperature-composition relationships of authigenic micaceous minerals in the Los Azufres geothermal system. Contrib. Mineral. Petrol. 100, 418–428.

Chan, Y.-C., Crespi, J.M., Hodges, K.V., 2000. Dating cleavage formation in slates and phyllites with the ^{40}Ar/^{39}Ar laser microprobe: an example from the western New England Appalachians, USA. Terra Nova 12, 264–271.

Chen, C.-H., Wang, C.-H., 1995. Explanatory notes for the metamorphic facies map of Taiwan. Special Report of Central Geological Survey 2, second ed. 51 pp.

Chen, C.-T., Chan, Y.-C., Lu, C.-Y., Simoes, M., Beyssac, O., 2011. Nappe structure revealed by thermal constraints in the Taiwan metamorphic belt. Terra Nova 23, 85–91.

Chen, C.-T., Chan, Y.-C., Lo, C.-H., Lee, J.-C., 2016a. Complex Accretionary History of Continental Margin Sediments in the Taiwan Orogen: Prolonged Wedge Thickening through Basal Accretion Revealed by Thermal-chronological Constraints from the Slate Terrain, 2016 Annual Meeting abstract, SE34-A023. Asia Oceania Geoscience Assembly.

Chen, C.-T., Chan, Y.-C., Lo, C.-H., Lu, C.-Y., Tang, J.-T., Lee, Y.-H., 2016b. Downward Thickening of Taiwan Mountain Belt: Revealed by Dating Rock Cleavage submitted for publication.

Clark, M.B., Fisher, D.M., 1995. Strain partitioning and crack-seal growth of chlorite-muscovite aggregates during progressive noncoaxial strain: an example from the slate belt of Taiwan. J. Struct. Geol. 17, 461–474.

Clark, M.B., Fisher, D.M., Lu, C.-Y., Chen, C.-H., 1993. Kinematic analyses of the Hsueshan Range, Taiwan: a large-scale pop-up structure. Tectonics 12, 205–217.

Evarts, R.C., Schiffman, P., 1983. Submarine hydrothermal metamorphism of the Del Puerto ophiolite, California. Am. J. Sci. 283, 289–340.

Fisher, D.M., Lu, C.-Y., Chu, H.-T., 2002. Taiwan Slate Belt: insights into the ductile interior of an arc-continent collision. In: Byrne, T.B., Liu, C.-S. (Eds.), Geology and Geophysics of an Arc-continent Collision, vol. 358. Geological Society of America Special Paper, Taiwan. Boulder, Colorado, pp. 93–106.

Fitz-Diaz, E., van der Pluijm, B., 2013. Fold dating: a new Ar/Ar illite dating application to constrain the age of deformation in shallow crustal rocks. J. Struct. Geol. 54, 174–179.

Fuller, C.W., Willett, S.D., Fisher, D., Lu, C.-Y., 2006. A thermomechanical wedge model of Taiwan constrained by fission-track thermochronometry. Tectonophysics 425, 1–24.

Furbish, W.J., 1975. Corrensite of deuteric origin. Am. Mineral. 60, 928–930.

Glodny, J., Lohrmann, J., Echtler, H., Gräfe, K., Seifert, W., Collao, S., Figueroa, O., 2005. Internal dynamics of a paleoaccretionary wedge: insights from combined isotope tectonochronology and sandbox modeling of the South-Central Chilean forearc. Earth Planet. Sci. Lett. 231, 23–39.

Harrison, T.M., Celerier, J., Aikman, A.B., Hermann, J., Heizler, M.T., 2009. Diffusion of ^{40}Ar in muscovite. Geochim. Cosmochim. Acta 73, 1039–1051.

Hodges, K.V., 2014. Thermochronology in orogenic systems. Treatise Geochemistry, second ed., pp. 281–308

Huang, C.-Y., Yuan, P.B., Tsao, S.-J., 2006. Temporal and spatial records of active arc-continent collision in Taiwan: a synthesis. Geol. Soc. Am. Bull. 118, 274–288.

Lee, J.-C., Angelier, J., Chu, H.-T., 1997. Polyphase history and kinematics of a complex major fault zone in the northern Taiwan mountain belt: the Lishan Fault. Tectonophysics 274, 97–115.

Lee, Y.-H., Byrne, T., Wang, W.-H., Lo, W., Rau, R.-J., Lu, H.-Y., 2015. Simultaneous mountain building in the Taiwan orogenic belt. Geology 43–5, 451–454.

Lin, A.T., Watts, A.B., Hesselbo, S.P., 2003. Cenozoic stratigraphy and subsidence history of the South China Sea margin in the Taiwan region. Basin Res. 15, 453–478.

Lo, C.-H., Onstott, T.C., 1995. Rejuvenation of K-Ar systems for minerals in the Taiwan mountain belt. Earth Planet. Sci. Lett. 131, 71–98.

Lo, C.-H., Chung, S.-L., Lee, T.-Y., Wu, G.-Y., 2002. Age of the Emeishan flood magmatism and relations to Permian-Triassic boundary events. Earth Planet. Sci. Lett. 198, 449–458.

Malavieille, J., 2010. Impact of erosion, sedimentation, and structural heritage on

the structure and kinematics of orogenic wedges: analog models and case studies. GSA Today 20, 4—10.

Merriman, R.J., Peacor, D.R., 1999. Very low-grade metapelites: mineralogy, microfabrics and measuring reaction progress. In: Frey, M., Robinson, D. (Eds.), Low-grade Metamorphism. Oxford, UK, Blackwell, pp. 10—60.

Mukherjee, S., 2011. Mineral fish: their morphological classification, usefulness as shear sense indicators and genesis. Int. J. Earth Sci. 100, 1303—1314.

Mulch, A., Cosca, M.A., Andresen, A., Fiebig, J., 2005. Time scales of deformation and exhumation in extensional detachment systems determined by high-spatial resolution in situ UV-laser $^{40}Ar/^{39}Ar$ dating. Earth Planet. Sci. Lett. 233, 375—390.

Odin, G.S., 35 collaborators, 1982. Interlaboratory standards for dating purposes. In: Odin, G.S. (Ed.), Numerical Dating in Stratigraphy, United Kingdom, pp. 123—149.

Passchier, C.W., Trouw, R.A.J., 2005. Microtectonics, second ed. Springer Verlag. 366 pp.

Renne, P.R., Mundil, R., Balco, G., Min, K., Ludwig, K.R., 2010. Joint determination of ^{40}K decay constants and $^{40}Ar^*/^{40}K$ for the Fish Canyon sanidine standard, and improved accuracy for $^{40}Ar/^{39}Ar$ geochronology. Geochim. Cosmochim. Acta 74, 5349—5367.

Schneider, S., Hammerschmidt, K., Rosenberg, C.L., 2013. Dating the longevity of ductile shear zones: insight from $^{40}Ar/^{39}Ar$ in situ analyses. Earth Planet. Sci. Lett. 369—370, 43—58.

Shau, Y.-H., Yang, H.-Y., 1987. Petrology of basaltic rocks from Junghua, Taoyuanhsien, northern Taiwan. Proc. Geol. Soc. China 30, 58—82.

Shau, Y.-H., Peacor, D.R., Essene, E.J., 1990. Corrensite and mixed-layer chlorite/corrensite in metabasalt from northern Taiwan: TEM/AEM, EMPA, XRD, and optical studies. Contrib. Mineral. Petrol. 105, 123—142.

Shyu, J.B.H., Sieh, K., Chen, Y.-G., 2005. Tandem suturing and disarticulation of the Taiwan orogen revealed by its neotectonic elements. Earth Planet. Sci. Lett. 233, 167—177.

Simoes, M., Avouac, J.P., Beyssac, O., Goffe, B., Farley, K.A., Chen, Y.-G., 2007. Mountain building in Taiwan: a thermokinematic model. J. Geophys. Res. 112, B11405.

Suppe, J., 1981. Mechanics of mountain building and metamorphism in Taiwan. Mem. Geol. Soc. China 4, 67—89.

Suppe, J., 1984. Kinematics of arc-continent collision, flipping of subduction and back-arc spreading near Taiwan. Mem. Geol. Soc. China 6, 21—33.

ten Grotenhuis, S.M., Trouw, R.A.J., Passchier, C.W., 2003. Evolution of mica fish in mylonitic rocks. Tectonophysics 372, 1—21.

Teng, L.S., 1990. Geotectonic evolution of late Cenozoic arc-continent collision in Taiwan. Tectonophysics 183, 57—76.

Teng, L.S., 1992. Geotectonic evolution of Tertiary continental margin basins of Taiwan. Petroleum Geol. Taiwan 27, 1—19.

Teng, L.S., Lin, A.T., 2004. Cenozoic tectonics of the China continental margin: insights from Taiwan. In: Malpas, J., Fletcher, C.J.N., Ali, J., Aitchison, J.C. (Eds.), Aspects of the Tectonic Evolution of China, vol. 226. Geological Society, London, Special Publications, pp. 313—332.

Tillman, K.S., Byrne, T.B., 1995. Kinematic analysis of the Taiwan slate belt. Tectonics 14, 322—341.

Wang, H.-H., 2011. Exhumation History of the Northern Hsuehshan Range and its Tectonic Implication [M.S. thesis]. National Chung-Cheng University, Chiayi, Taiwan, 46 pp.

Wells, M.L., Spell, T.L., Hoisch, T.D., Arriola, T., Zanetti, K.A., 2008. Laser-probe $^{40}Ar/^{39}Ar$ dating of strain fringes: mid-Cretaceous synconvergent orogen-parallel extension in the interior of the Sevier orogen. Tectonics 27, TC3012.

Yang, H.-Y., Shau, Y.-H., 1988. Occurrence of pumpellyite-bearing basaltic tuffs in Hsuehshan Range. Proc. Geol. Soc. China 31, 24—32.